Available online at www.sciencedirect.com
SCIENCE DIRECT®
Journal of Sound and Vibration 289 (2006) 382–412
JOURNAL OF SOUND AND VIBRATION
www.elsevier.com/locate/jsvi

Experimental modal analysis of three small-scale vibration isolator models

J.A. Forrest*

Maritime Platforms Division, Defence Science & Technology Organisation, PO Box 4331, Melbourne, VIC 3001, Australia

Received 21 May 2004; received in revised form 1 February 2005; accepted 8 February 2005
Available online 28 April 2005

Abstract

This paper discusses the experimentally measured free–free dynamics of three small-scale vibration isolator models: two single-stage isolators and one two-stage isolator. The first comprises two steel plates and one rubber element, the second two steel plates and four rubber elements, and the third three steel plates and eight rubber elements. The natural frequencies, mode shapes and associated modal damping derived from curve-fitting procedures applied to the measured frequency-response functions (FRFs) are presented. The modal behaviour of the isolators is more complicated than might at first be assumed, a major feature being significant coupling between different degrees of freedom. The modal properties can be used to reconstruct a complete set of FRFs for the isolator, including FRFs which were not measured directly. Vibration isolators are often characterised through the use of four-pole parameters or various transmissibilities, and so methods for calculating these parameters from the reconstructed FRFs are also given.

1. Introduction

This paper is concerned with the dynamics of three small-scale vibration isolator models, two single-stage ones and one two-stage one, consisting of various combinations of rubber and steel elements. The work described is part of a collaborative programme of measurements undertaken

*Fax: +61 3 9626 8373.
E-mail address: james.forrest@dsto.defence.gov.au.

0022-460X/$ - see front matter © 2005 Elsevier Ltd. All rights reserved.
doi:10.1016/j.jsv.2005.02.022

by the Defence Science and Technology Organisation (DSTO), Australia, to provide data for comparison to mathematical models developed by Defence Research & Development Canada (DRDC). Measurements and analysis based on a simple peak-picking approach for the two single-stage isolator models are presented in Forrest [1], while more detailed modal analysis of the two-stage isolator is given in Forrest [2]. The eventual aim is to obtain accurate models of real vibration-isolator assemblies that could form part of an overall model for structural vibration transmission in ships or submarines. An overview of foundation design issues, including isolator impedance is given in Tso et al. [3].

The current work investigates isolator dynamics in the (approximately) free–free state. This has the advantage that frequency-response functions (FRFs) can be easily measured in all directions, with no constraints on any of the translational or rotational modes, or on coupling between motion in different directions. Modal analysis of the measured FRFs can give clear insight into an isolator's dynamics and it is a simple procedure to calculate the isolator's response to any generalised loading condition from the modal properties (see Refs. [4] or [5]). However, the dynamic characteristics of rubber depend on static pre-load, temperature and the frequency and amplitude of vibration, none of which are readily controlled in a free–free situation. Lindley [6] discusses these issues with others, Kari et al. [7] discuss temperature effects and Dickens [8] discusses static load effects. Warley [9] gives a method for selecting rubber materials for a particular isolator performance. Characterisations of the dynamics of an isolator include its blocked impedance as described in Verheij [10], or its four-pole parameters as described in Norwood and Dickens [11]. A method and testing machine to determine the four-pole parameters is described by Dickens and Norwood [12]. While these approaches can take the effects of various conditions into account, they deal either with the basic material properties of rubber or with one-dimensional translational dynamics, usually in the axial direction alone, where coupling between directions is assumed to be negligible.

The following sections describe the isolator models, the measurement method, the modal analysis of the measured FRFs, and the derivation of the four-pole parameters and some transmissibilities from the reconstructed FRFs.

2. Experimental equipment and method

The dimensions of the three isolator models examined are given in Figs. 1–3. The three principal directions X (lateral), Y (transverse) and Z (axial) are indicated in the top views of each figure. The first single-stage isolator, which will be referred to as the "small" isolator, is shown in Fig. 1. It consists of two small steel plates and one rubber element. Fig. 2 shows the second single-stage isolator, which will be referred to as the "medium" isolator. It consists of two steel plates and four rubber elements. The two-stage isolator, consisting of three steel plates and eight rubber elements, is shown in Fig. 3. As shown, the plates each have three threaded holes in each edge, and the end plates have one threaded hole in their outward faces. These holes allow screws to be used to attach suspension strings to the isolators. Each small plate has a mass of 640 g, each larger plate is 2687 g, while each rubber element is 31 g. This gives total masses of about 1.3 kg for the small isolator, 5.5 kg for the medium isolator, and 8.3 kg for the two-stage isolator.

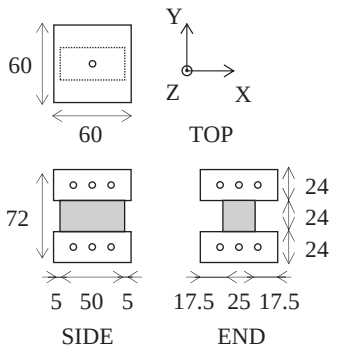

Fig. 1. The construction and dimensions (mm) of the small vibration isolator model, showing the coordinate directions X, Y and Z in the top view.

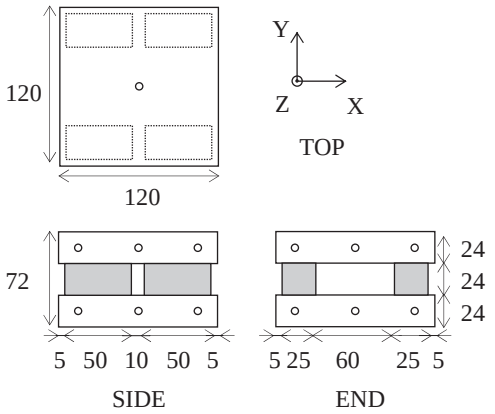

Fig. 2. The construction and dimensions (mm) of the medium vibration isolator model.

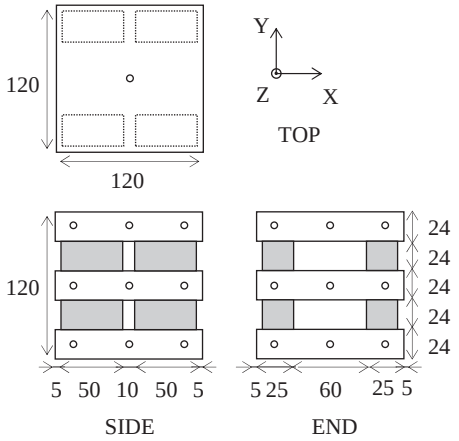

Fig. 3. The construction and dimensions (mm) of the two-stage vibration isolator model.

Fig. 4 shows all three isolator models set up for three different sets of measurements in each of the principal directions. The isolators were suspended by one or two strings as shown, each string consisting of a few strands of light 20 lb fishing line, with a hanging length of about 800 mm, which reasonably approximates the free–free state. Rigid-body modes with zero frequency are replaced by similar free vibration modes with low natural frequencies of a few Hz, which thus do not interfere with the modes of interest. These modified rigid-body modes include translations such as the pendulum mode of an isolator as a mass on its suspension string, or rotations due to the twisting of the string acting as a torsional spring, or rocking rotations of the isolator about its suspension attachment point acting as a pivot. These particular modes are easy to induce by hand, and good estimates of their periods can be obtained by counting oscillations and timing with a stopwatch.

For each measurement set, the suspended isolator model was excited by a 0.24 mV/N impulse hammer with a teflon tip as indicated by the arrows in Fig. 4. Small 10 mV/g accelerometers of mass less than 3 g, secured with wax, were used to measure the response of the isolator at corner positions on each plate as illustrated in Fig. 4. With the assumption that the plates are effectively

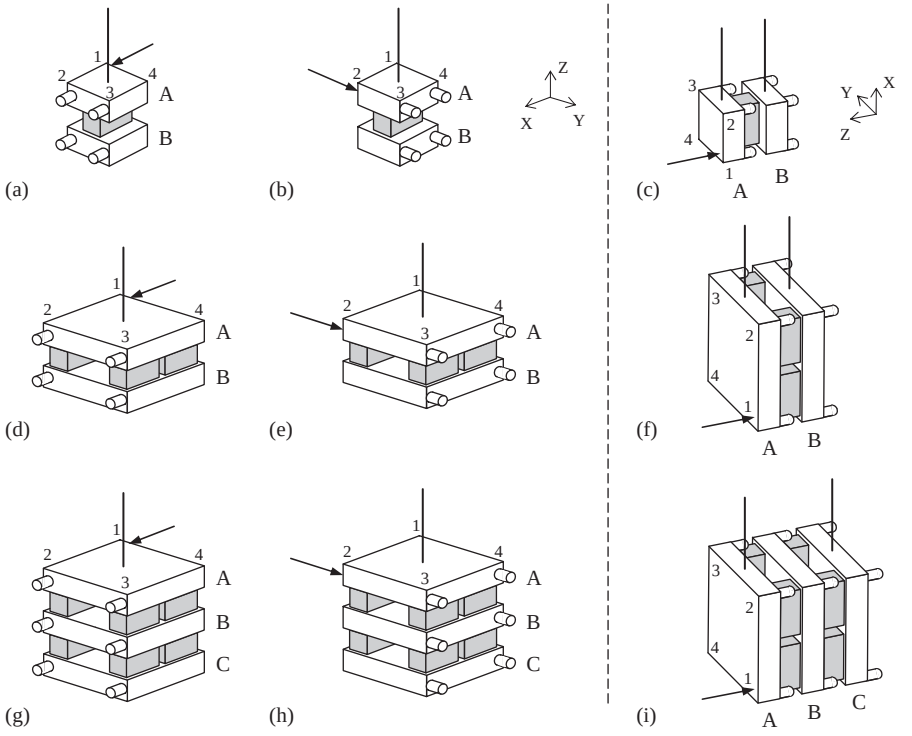

Fig. 4. The setups for measurements for (a)–(c) the small isolator, (d)–(f) the medium isolator and (g)–(i) the two-stage isolator in the three principal directions. The first setup in each row is for measurement in the lateral (X) direction, the second in the transverse (Y) direction, and the third in the axial (Z) direction. The plates are labelled A and B (and C for the two-stage case) while the four corners of each plate are labelled 1, 2, 3 and 4. One vertical suspension string was used for measurements in the X- or Y-direction, while two strings were used for those in the Z-direction. The accelerometers are shown as small cylinders; those at position 4 on the plates in (c), (f) and (i) are obscured. The isolators were excited in each case by the modal hammer applied as indicated by the arrows.

rigid in the relatively low-frequency range of interest, this arrangement of accelerometers allows a full picture of the isolator dynamics in the given direction to be obtained. Data was acquired using an HP 3566A FFT analyser controlled by a laptop PC, onto which the measured FRFs were saved. Because the measured signals were transient and decayed quickly, no windowing was necessary. Each saved FRF was based on the average of five measurements.

3. Modal analysis

A quick way to estimate natural frequencies and mode shapes is through modal peak picking as described in the HP application note [13]. At a resonance of a lightly damped system, the imaginary parts of its FRFs will become maximum while the real parts become zero, since the phase at resonance is $\pm 90^{\circ}$. Plotting the imaginary parts of the FRFs thus allows an estimate for the natural frequencies to be made from the position of the peaks, and for the mode shapes from the relative heights of the peaks for a given resonance across all the FRFs. However, this method is not particularly accurate, especially when the damping becomes high or there are closely spaced modes, both of which can result in the FRFs having significantly non-zero real parts at the resonances in question. Peak picking is not suited to determining modal damping either.

Manual peak picking was therefore used as a way to understand the responses before processing in more detail using the curve-fitting routines in the ICATS MODENT modal-analysis software package. The results tabulated in the following sections were calculated using the nonlinear least-squares multi-FRF methods NLLS-1 and NLLS-2, which analyse all FRFs at once, but require initial guesses for natural frequencies. Peak picking from imaginary parts was particularly useful to estimate these frequencies in cases of closely spaced modes, because the signs of the peaks alternate on at least one coordinate's FRF plot, allowing the modes to be clearly distinguished. Since the MODENT peak-picking function only allows an FRF magnitude plot, the imaginary parts were plotted and analysed separately, and are presented in the following sections.

The mode shapes were deduced from both the plots of FRF imaginary parts and animation using the MODESH component of the ICATS suite. For particularly complicated modes, snapshots of the mode-shape animations are given as well as modal data and mode-shape schematics. Numerical data for the mode-shape vectors appears in Appendix A.

A driving-point FRF is required for curve-fitting approaches such as those used by MODENT to work. It is assumed that at the relatively low frequencies under consideration, the steel plates are rigid, so that the accelerometer in line with the force's line of action gives the driving-point response. These are the accelerometers at A2 in Fig. 4(a), (d) and (g); at A3 in Fig. 4(b), (e) and (h); and at A1 in Fig. 4(c), (f) and (i).

3.1. Results for the small isolator

The small isolator represents the simplest configuration of the three isolators examined. The modes observed happen to match the simple set of modes that might be expected, namely one translational mode in each principal direction, and one rotational mode about each principal axis.

The imaginary parts of the FRFs measured in the X-direction for the small isolator are given in Fig. 5, labelled with the position of the accelerometer from whose response they are derived. Examining all four plots reveals peaks at about 40 and 100 Hz, apart from some noisy peaks below 20 Hz which are due to the modified rigid-body modes discussed in Section 2. As an example of using the relative peak sizes to deduce a mode shape, the 40 Hz mode has A2 and A3 moving in equal and opposite directions, and B2 and B3 equal and opposite but also opposite to A2 and A3. This means that plate A is rotating in the opposite direction to plate B, so the mode is the rotational mode about the Z-axis. Similarly, the 100 Hz mode is the translational mode in the X-direction. The more precise natural frequencies f_n as well as modal damping loss factors η_n calculated by MODENT curve-fitting are given in Table 1. Schematics of these mode shapes are given in Fig. 6, which is referenced by Table 1.

The imaginary parts of the Y-direction FRFs are given in Fig. 7, showing peaks at about 40 and 94 Hz. The modal parameters from the FRFs are given in Table 2. Once again, there is the rotational mode about Z as detected previously, plus a new translational mode. The different measurements in Tables 1 and 2 of the same rotational mode can give an indication of the accuracy of the calculated modal parameters. While the two values of the natural frequency are within 0.3% of each other, the two values of the modal damping are more than 6% apart, a much higher degree of uncertainty.

The imaginary parts of the Z-direction FRFs are given in Fig. 8. There are two clear natural frequencies on all the FRFs, namely those at about 49 and 134 Hz. Examining the signs of the imaginary parts, it is easy to see that the first is the opposite rotation of the two plates about the X-axis, while the second is the opposite translation of the two plates in the Z-direction.

There is also a cluster of overlapping peaks at and below about 100 Hz. The various sign combinations result in B1 and B3 clearly showing three distinct peaks at about 93, 96 and 100 Hz. The details of these modes, along with the other two, appear in Table 3. Modes 2 and 4 both

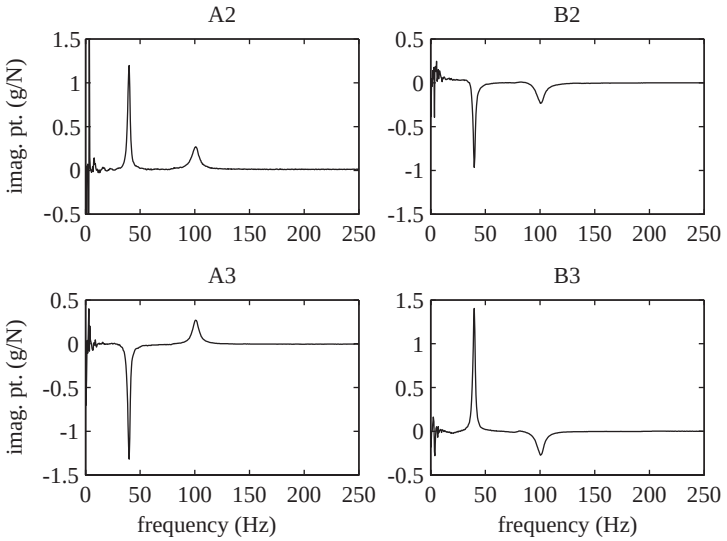

Fig. 5. The imaginary parts of the FRFs measured as depicted in Fig. 4(a) for the small isolator in the X-direction.

Table 1
Natural frequencies, modal damping and corresponding mode shapes for the small isolator in the X-direction

Mode	f_n (Hz)	η_n	Description	Figure
1	39.9	0.0633	Rotation about Z	6(a)
2	100.6	0.0867	Translation in X	6(b)

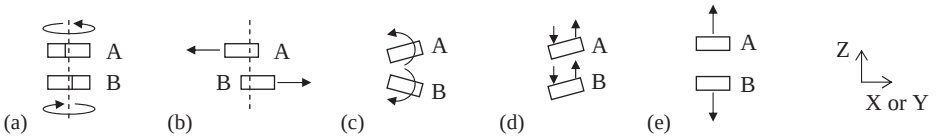

Fig. 6. Modes observed for the small isolator include (a) rotation about Z, (b) translation in X or Y, (c) rotation about X or Y, (d) equal tilting of both plates about X or Y, and (e) translation in Z.

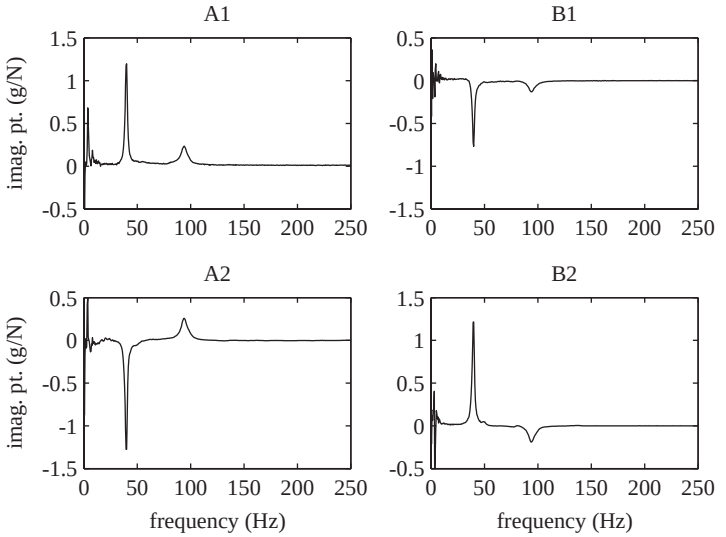

Fig. 7. The imaginary parts of the FRFs measured as depicted in Fig. 4(b) for the small isolator in the Y-direction.

Table 2
Natural frequencies, modal damping and corresponding mode shapes for the small isolator in the Y-direction

Mode	f_n (Hz)	η_n	Description	Figure
1	39.8	0.0594	Rotation about Z (same as mode 1, Table 1)	6(a)
2	94.4	0.1137	Translation in Y	6(b)

involve equal tilting of the plates as depicted in Fig. 6(d) (about a different axis in each case). At first this looks something like a rigid-body rotation about X or Y (as the case may be), but the modified rigid-body modes due to the suspension of the isolators are known to have much lower

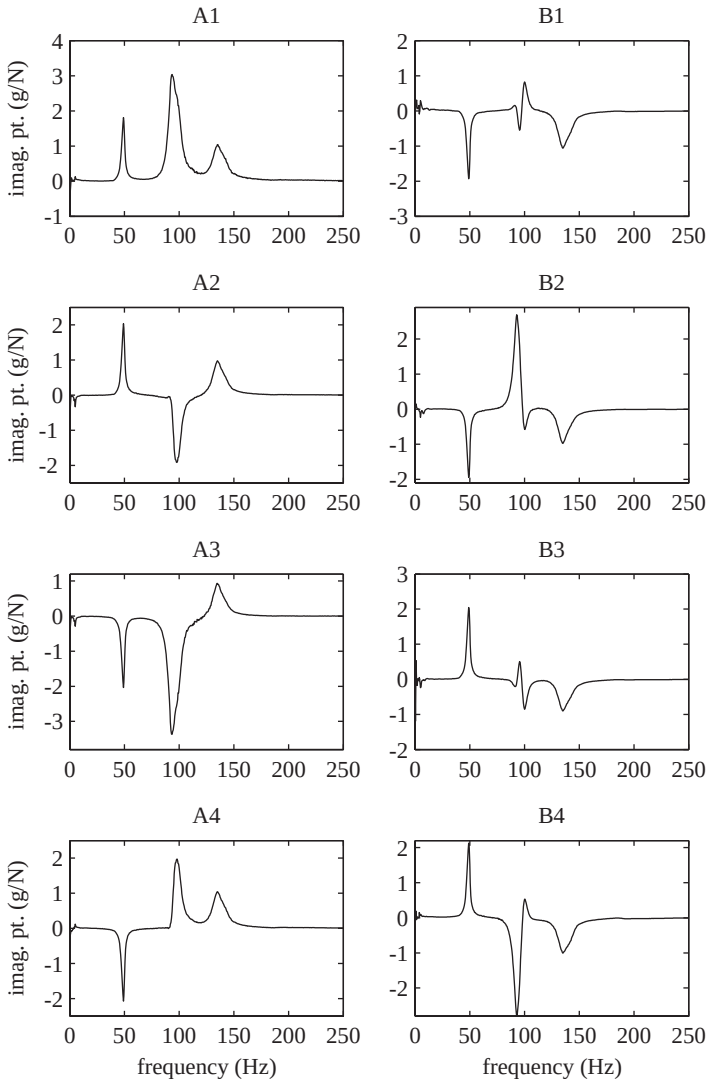

Fig. 8. The imaginary parts of the FRFs measured as depicted in Fig. 4(c) for the small isolator in the Z-direction.

Table 3
Natural frequencies, modal damping and corresponding mode shapes for the small isolator in the Z-direction

Mode	f_n (Hz)	η_n	Description	Figure
1	49.1	0.0650	Rotation about X	6(c)
2	93.1	0.0760	Equal tilting about X with some diagonal rotation (mode 2, Table 2)	6(d), 6(b), 9
3	95.8	0.0705	Rotation about Y	6(c)
4	99.6	0.0675	Equal tilting about Y (mode 2, Table 1)	6(d), 6(b)
5	134.3	0.1046	Translation in Z	6(e)

frequencies. However, if the diagram of equal tilting in Fig. 6(d) is turned slightly so that the plates are horizontal, it becomes clear that it has the same relative plate motion as the diagram of the translational modes in Fig. 6(b). Thus the equal-tilting modes are manifestations in the Z-direction of translational modes in the X- or Y-directions. Equal tilting about X or Y results in plate translation in Y or X respectively, and vice versa, due to the coupling effects introduced by the resultant deformation of the rubber element in each case. This is borne out by the similar frequencies of these modes across the tables of results.

Mode 2 in Table 3 is complicated by additional rotation of the plates about their diagonals as illustrated by the animation snapshot of Fig. 9. This is perhaps why it is not as good a match to its corresponding translation mode as mode 4 is—there are two effects occurring which could not be separated by the analysis employed.

3.2. Results for the medium isolator

The modes of the medium isolator did not correspond particularly closely with principal-axis translations and rotations, or even with modes of the other two isolators. No axial translation mode was observed, nor were there straightforward correspondences between particular modes in different directions.

The imaginary parts of the FRFs measured for the medium isolator in the X-direction are given in Fig. 10. There is a cluster of three peaks between about 60 and 75 Hz, and a very low peak at about 116 Hz. The detailed results are given in Table 4, with schematics of the modes displayed in Fig. 11. It is interesting to note that both modes 1 and 2 are rotations about Z, but are clearly distinct in the imaginary-part plots, particularly those for A3 and B3. Mode 4 is a highly complex rotation about Z, resulting in significant phase delay between the motions of the two measured sides (A2–B2 and A3–B3): they are not exactly in-phase or out-of-phase with each other, a feature particularly noticeable in the animation of the mode. This is possible despite each end plate being rigid, because the two corners represent 2 dof and so can move independently. Mode 3 has the character of a translation in X, because A2 and A3 move in the same direction while B2 and B3 move in the opposite direction, but with a superimposed rotation as illustrated in Fig. 12.

As can be seen in Fig. 13, the situation for the Y-direction FRFs is similar to that for the X-direction, with a cluster of peaks between 60 and 75 Hz, and one, or maybe more, very small peaks above 100 Hz. The detailed results are given in Table 5, and the first two schematics of Fig. 11 again apply. While there is an almost 3% difference in the calculated natural frequencies, it seems probable that the mode 1 rotation about Z is the same as the mode 1 rotation observed in the X-direction and given in Table 4. The next two modes are more ambiguous. Their frequencies are within 1.5% of the modes with the same numbers in Table 4. However, mode 2 appears here as

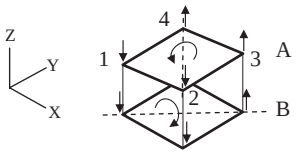

Fig. 9. Snapshot of mode 2 in the Z-direction for the small isolator, showing the rotations about A2–A4 and B1–B3 superimposed on the tilting of the plates about X.

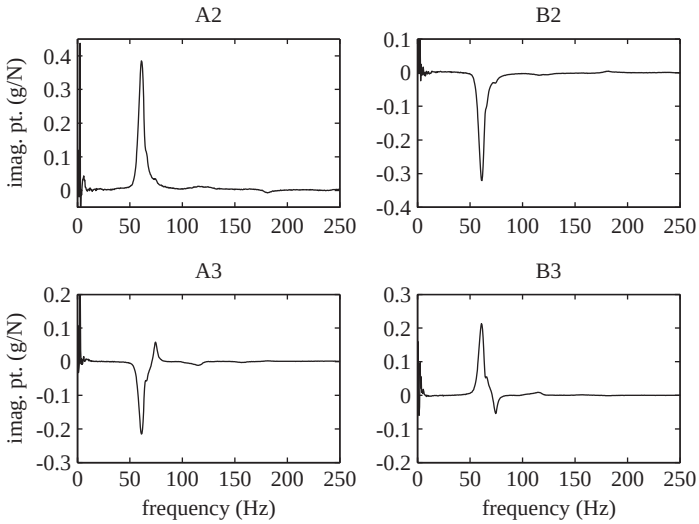

Fig. 10. The imaginary parts of the FRFs measured as depicted in Fig. 4(d) for the medium isolator in the X-direction.

Table 4
Natural frequencies, modal damping and corresponding mode shapes for the medium isolator in the X-direction

Mode	f_n (Hz)	η_n	Description	Figure
1	60.9	0.1130	Rotation about Z	11(a)
2	64.0	0.0366	Rotation about Z	11(a)
3	74.4	0.0594	Translation in X with greater motion on A3–B3 side	11(b), 12
4	116.3	0.1020	Rotation about Z with phase delay between the two sides	11(a)

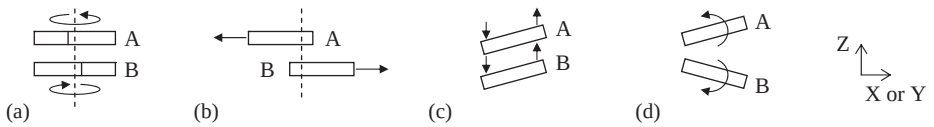

Fig. 11. Modes observed for the medium isolator include (a) rotation about Z, (b) translation in X or Y, (c) equal tilting of both plates about X or Y, and (d) rotation about X or Y.

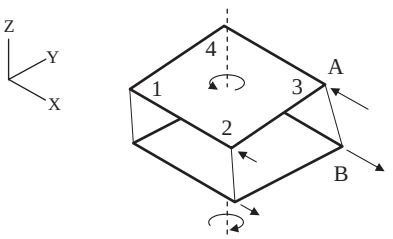

Fig. 12. Snapshot of mode 3 in the X-direction for the medium isolator, showing how the uneven translations in X on either side result in rotation of the plates.

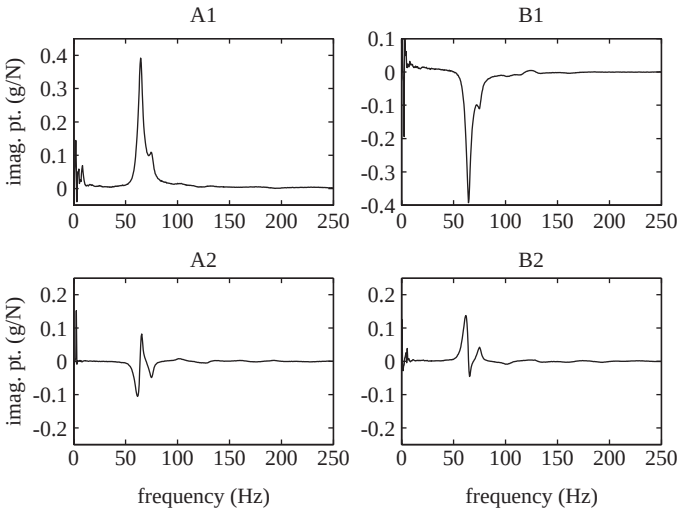

Fig. 13. The imaginary parts of the FRFs measured as depicted in Fig. 4(e) for the medium isolator in the Y-direction.

Table 5
Natural frequencies, modal damping and corresponding mode shapes for the medium isolator in the Y-direction

Mode	f_n (Hz)	η_n	Description	Figure
1	62.6	0.1586	Rotation about Z (same as mode 1, Table 4)	11(a)
2	64.6	0.0669	Translation in Y with phase delay between the two sides (mode 2, Table 4)	11(b)
3	75.5	0.0580	Rotation about Z (mode 3, Table 4)	11(a)
4	102.4	0.0775	Translation in Y	11(b)

a translation in Y (albeit noticeably complex when animated), but as a rotation about Z in the X-direction measurements. Likewise, mode 3 appears as a rotation about Z here, but as a translation in X in Table 4. Neither of these two modes is a pure translation, and so the translation in X results in some rotation being detected in the Y-direction (mode 3), and vice versa (mode 2). Nevertheless, mode 4 at about 102 Hz does appear to be pure translation in Y, with no corresponding response detected in the X-direction.

Fig. 14 gives the imaginary parts of the Z-direction FRFs. Detailed results are given in Table 6, and the schematics of Fig. 11 apply. The peaks for the first two modes at about 66 and 74 Hz are quite small, and correspond to two equal-tilting modes, the first about X, the second about Y. As discussed for the similar modes in the case of the small isolator, these modes are manifestations in the Z-direction of translations in Y or X respectively, showing that coupling between motion in the different directions is also important for the medium isolator. The other modes are self-explanatory, with Fig. 15 providing extra illustration of the less easily categorised modes 3 and 6. What is perhaps remarkable is that no mode of simple translation in Z is observed in the frequency range considered. It is clear from all the results that the dynamics of the medium isolator give rise to numbers of similar, relatively complicated, modes with only subtle differences.

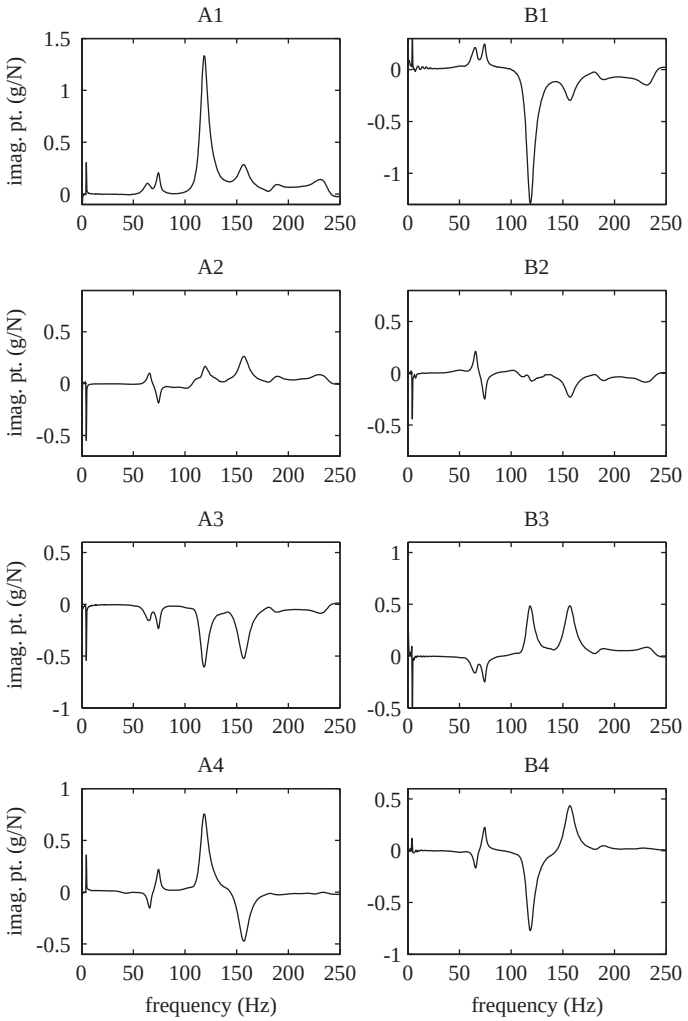

Fig. 14. The imaginary parts of the FRFs measured as depicted in Fig. 4(f) for the medium isolator in the Z-direction.

Table 6
Natural frequencies, modal damping and corresponding mode shapes for the medium isolator in the Z-direction

Mode	f_n (Hz)	η_n	Description	Figure
1	65.7	0.0794	Equal tilting about X (same as mode 2, Table 5)	11(c), 11(b)
2	74.4	0.0633	Equal tilting about Y (same as mode 3, Table 4)	11(c), 11(b)
3	118.2	0.0758	Rotation about Y with some rotation about 2–4 diagonals, A2 and B2 hardly move	11(d), 15(a)
4	156.6	0.0798	Rotation about X	11(d)
5	189.8	0.0585	Rotation about X with some rotation about 1–3 diagonals	11(d)
6	236.3	0.0651	Rotation about X with some rotation about 2–4 diagonals, A4 and B4 hardly move	11(d), 15(b)

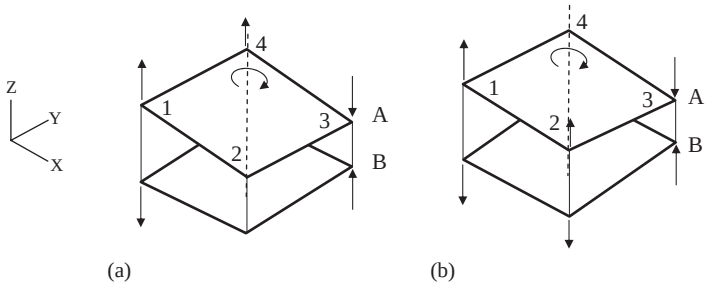

Fig. 15. Snapshots of (a) mode 3 and (b) mode 6 in the Z-direction for the medium isolator. Corners A2 and B2 in (a) and A4 and B4 in (b) move very little, resulting in (a) having the character of a rotation about Y and (b) that of one about X, despite the diagonal rotations being about the 2–4 diagonals in both cases.

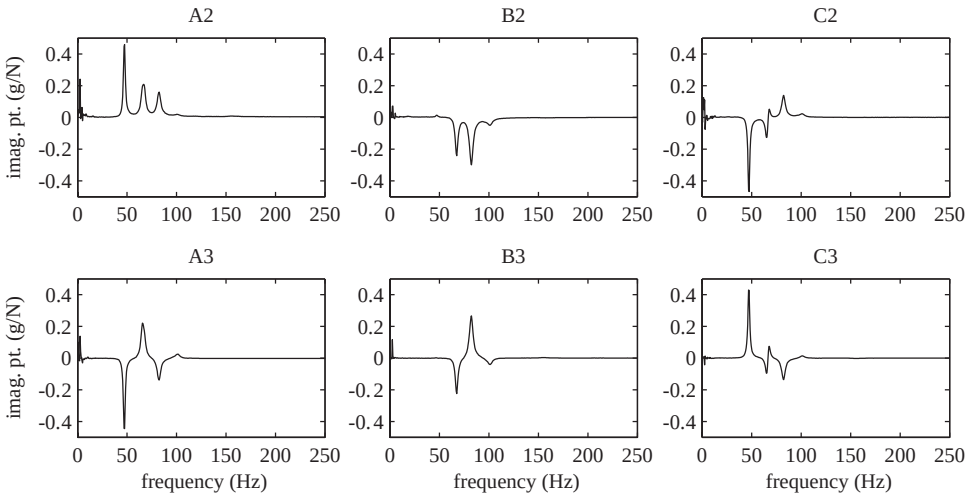

Fig. 16. The imaginary parts of the FRFs measured as depicted in Fig. 4(g) for the two-stage isolator in the X- direction.

3.3. Results for the two-stage isolator

The addition of the second stage in the two-stage isolator introduces extra degrees of freedom. Despite this and the similarity in design to the medium isolator, the modes observed are more easily categorised as principal-axis translations and rotations than the medium isolator's. The main distinguishing feature of the two-stage isolator is that these modes can be of antisymmetric or symmetric type.

The imaginary parts of the FRFs measured for the two-stage isolator in the X-direction are given in Fig. 16. Examining all six plots reveals peaks at five frequencies of about 47, 65, 67, 82 and 101 Hz. The detailed modal data is given in Table 7, and schematics of the mode shapes are given in Fig. 17. The 47 and 82 Hz modes illustrate the two mode types. The relative peak sizes for mode 1 (47 Hz) show A2 and A3 moving in equal and opposite directions, nearly zero motion of

Table 7
Natural frequencies, modal damping and corresponding mode shapes for the two-stage isolator in the X-direction

Mode	f_n (Hz)	η_n	Description	Figure
1	47.2	0.0464	Antisymmetric rotation about Z	17(a)
2	65.5	0.0596	Antisymmetric translation in X	17(b)
3	67.5	0.0518	Symmetric translation in X	17(c)
4	82.3	0.0528	Symmetric rotation about Z	17(d)
5	101.7	0.0601	Symmetric translation in X with small rotation of plate A about Z	17(c)

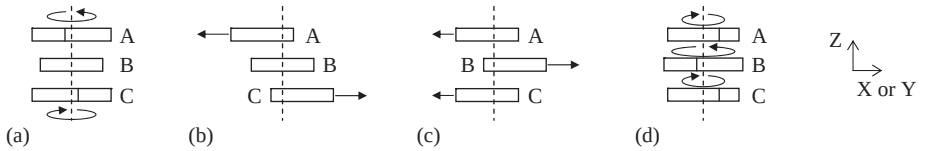

Fig. 17. Modes observed for the two-stage isolator in the X- and Y-directions include (a) antisymmetric rotation about Z, (b) antisymmetric translation in X or Y, (c) symmetric translation in X or Y, and (d) symmetric rotation about Z.

B2 and B3, and C2 and C3 equal and opposite but also opposite to A2 and A3. Thus plate A is rotating in the opposite direction to plate C while plate B is stationary, an antisymmetric rotational mode about Z. By similar reasoning, mode 4 (82 Hz) has plates A and C rotating in the same direction, with plate B rotating in the opposite direction with greater magnitude, giving a symmetric rotational mode about Z. Modes 3 and 5 are very similar to each other, as is the case with several of the medium isolator's modes. Modes 2 and 3 are very close in frequency and are only clearly discernible as separate peaks on the FRF imaginary parts for C2 and C3, which demonstrates the value of these plots.

Fig. 18 shows the imaginary parts of the Y-direction FRFs. The modal parameters are detailed in Table 8. Once again there are five modes, with the two rotational modes (1 and 4) being the same modes as detected in the X-direction, and with the translational modes being of similar type to the ones in the X-direction. Thus the schematics of Fig. 17 again apply to the mode-shape descriptions. Mode 5, which appears as very small peaks on the plots of imaginary parts, combines a rotation of plate A with the overall symmetric translation. This is illustrated in the snapshot of Fig. 19.

The Z-direction FRFs' imaginary parts are shown in Fig. 20. The detailed results are given in Table 9 and the schematics of the corresponding mode shapes appear in Fig. 21. Modes 4 and 5 are very similar antisymmetric translations with superimposed rotations. In mode 4, the moving plates A and C exhibit some rotation about Y as well as the main translation in the Z-direction, while in mode 5 they exhibit some rotation about their 1–3 diagonals as well as the translation. This is illustrated in Figs. 22(a) and (b), respectively.

The tilting modes (modes 1 and 2) have all three plates rotating equally and in the same direction around either the X- or Y-axis. If, as for the similar modes observed for the small and medium isolators, the depiction of these tilting modes as shown in Fig. 21(a) is rotated a little so

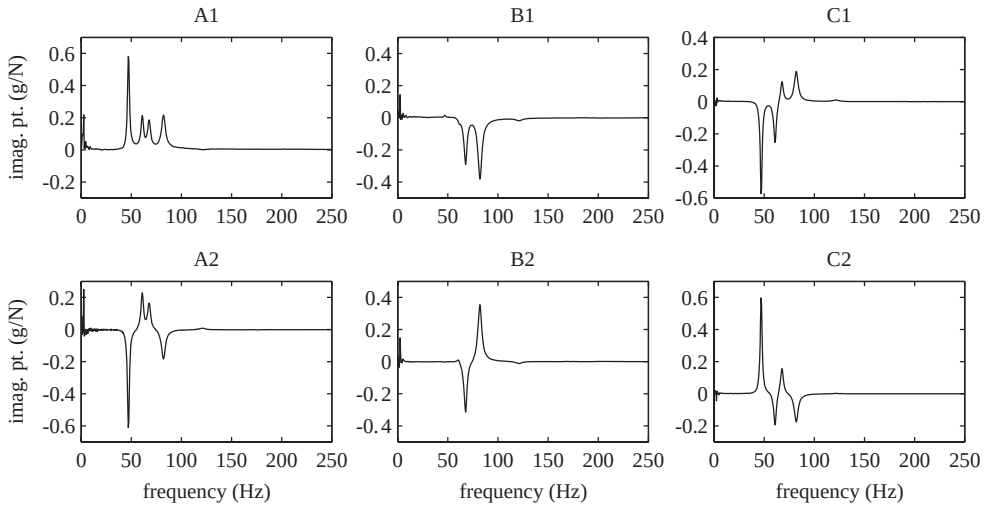

Fig. 18. The imaginary parts of the FRFs measured as depicted in Fig. 4(h) for the two-stage isolator in the Y-direction.

Table 8
Natural frequencies, modal damping and corresponding mode shapes for the two-stage isolator in the Y-direction

Mode	f_n (Hz)	η_n	Description	Figure
1	47.2	0.0470	Antisymmetric rotation about Z (same as mode 1, Table 7)	17(a)
2	61.0	0.0576	Antisymmetric translation in Y	17(b)
3	67.9	0.0548	Symmetric translation in Y	17(c)
4	82.1	0.0570	Symmetric rotation about Z (same as mode 4, Table 7)	17(d)
5	121.3	0.0726	Symmetric translation in Y with large rotation of plate A about Z	17(c), 19

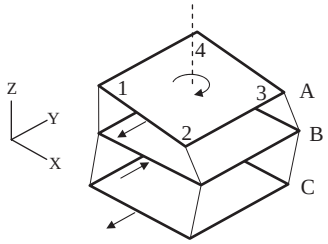

Fig. 19. Snapshot of mode 5 in the Y-direction for the two-stage isolator, showing the rotation of plate A superimposed on the underlying symmetric translation.

that the plates are horizontal, it matches the depiction of the antisymmetric translation modes shown in Fig. 17(b). As expected, the natural frequencies of these two modes match those of the corresponding translation modes listed in Tables 7 and 8 (mode 2 in each table). Thus the

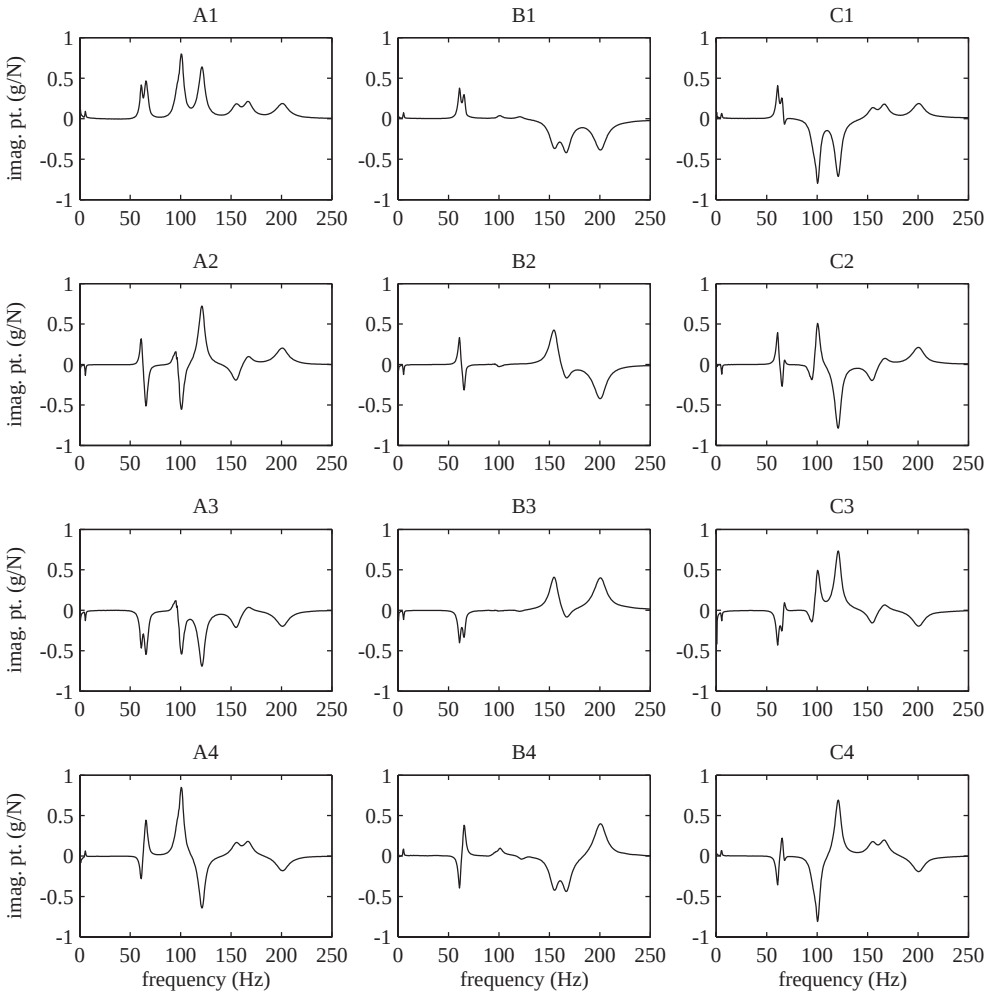

Fig. 20. The imaginary parts of the FRFs measured as depicted in Fig. 4(i) for the two-stage isolator in the Z-direction.

Z-direction equal-tilting modes correspond to antisymmetric translation modes in the X- or Y-directions. Similarly, the antisymmetric rotations about X and Y (modes 3, 6 and 7) depicted by Fig. 21(b) have frequencies very close to those for symmetric translations in Y or X, respectively. The translations of plates A and C in X or Y can cause rotations about Y or X, or vice versa, due to coupling through the rubber elements. Even though plate B is moving in the horizontal plane in symmetric translation, it does not register any rotation measurable in the Z-direction, because the rubber–element coupling forces on either face have equal and opposite Z-components, due to the opposite rotations of plates A and C. Therefore, these antisymmetric rotational modes most probably correspond to symmetric translation modes in the X- or Y-directions. This shows that there is significant coupling between the three principal directions for the two-stage isolator.

Table 9
Natural frequencies, modal damping and corresponding mode shapes for the two-stage isolator in the Z-direction

Mode	f_n (Hz)	η_n	Description	Figure
1	61.1	0.0515	Equal tilting about X (mode 2 in Table 8)	21(a), 17(b)
2	65.7	0.0517	Equal tilting about Y (mode 2 in Table 7)	21(a), 17(b)
3	67.6	0.0526	Antisymmetric rotation about Y with some rotation of plate B (mode 3 in Table 7)	21(b), 17(c)
4	93.0	0.1110	Antisymmetric translation in Z with some rotation about Y	21(c), 22(a)
5	98.3	0.0796	Antisymmetric translation in Z with some rotation about the 1–3 diagonals	21(c), 22(b)
6	100.6	0.0558	Antisymmetric rotation about Y (mode 5 in Table 7)	21(b), 17(c)
7	121.2	0.0621	Antisymmetric rotation about X (mode 5 in Table 8)	21(b), 17(c)
8	155.3	0.0703	Symmetric rotation about Y	21(d)
9	166.9	0.0658	Symmetric translation in Z with small rotation of plate B about Y	21(e)
10	200.8	0.0743	Symmetric rotation about X	21(d)

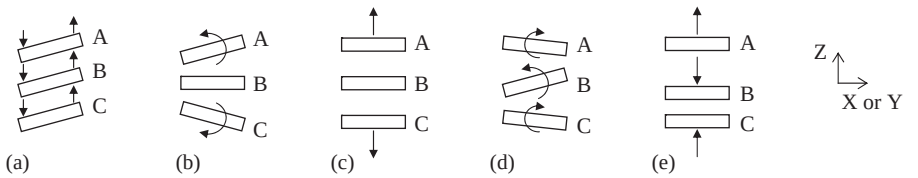

Fig. 21. Modes observed for the two-stage isolator in the Z-direction include (a) equal tilting of all plates about X or Y, (b) antisymmetric rotation about X or Y, (c) antisymmetric translation in Z, (d) symmetric rotation about X or Y, and (d) symmetric translation in Z.

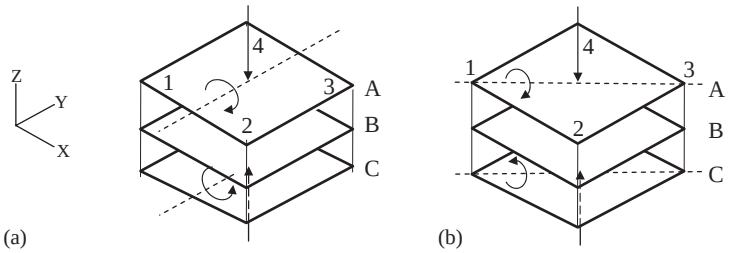

Fig. 22. Snapshots of (a) mode 4 and (b) mode 5 in the Z-direction for the two-stage isolator. In both cases the predominant motion is antisymmetric translation in Z, but there is some superimposed rotation of plates A and C about Y in (a) and about the 1–3 diagonals in (b).

4. Four-pole parameters and transmissibilities from modal data

FRFs are the most general characterisation of dynamic response and can easily be manipulated to obtain responses under specific conditions. The FRF for the response at any of the nodes used in the measurements to excitation at any node can be generated from the natural frequencies and

mode shapes obtained by modal analysis. The vector of nodal displacements **X** is related to the vector of forces **F** acting at the nodes by

$$\mathbf{X} = [\mathbf{H}]\mathbf{F}, \tag{1}$$

where [**H**] is the matrix of FRFs between the individual forces and displacements. Ewins [4] shows how to derive this FRF matrix from the modal properties. The final result is

$$[\mathbf{H}] = [\mathbf{\Phi}][\mathrm{diag}(\lambda_r^2 - \omega^2)]^{-1}[\mathbf{\Phi}]^{\mathrm{T}} = [\mathbf{\Phi}][\mathrm{diag}(1/(\lambda_r^2 - \omega^2))][\mathbf{\Phi}]^{\mathrm{T}}, \tag{2}$$

where [**Φ**] is the matrix of mode shapes as columns, and the central matrix is diagonal with elements being the differences between the corresponding natural frequencies squared λ_r^2 (r the mode number) and the angular frequency squared ω^2. The natural frequencies include the modal damping expressed as the loss factor η_r such that $\lambda_r^2 = \omega_r^2(1 + \mathrm{i}\eta_r)$, where ω_r is the real-number angular natural frequency calculated from modal analysis.

Fig. 23 compares the reconstructed driving-point FRF, calculated using Eq. (2), to the original measured driving-point FRF in the Z-direction for the two-stage isolator with a force applied at corner A1. The agreement between the measured and reconstructed FRFs is quite good, especially between 50 and 150 Hz. Of course, the reconstructed FRF does not include any of the modified rigid-body modes, and the residual effects of these may be one of the sources of mismatch between the two FRFs. Another factor is that the modal parameters are the best fit across the full set of 12 measured FRFs, not just the driving-point one. Nevertheless, the reconstructed FRF appears to be accurate, and the lack of rigid-body modes in the summation would not detract from the use of such FRFs to determine the behaviour of an isolator as a mount for a machine on a foundation, where such modes would be constrained anyway.

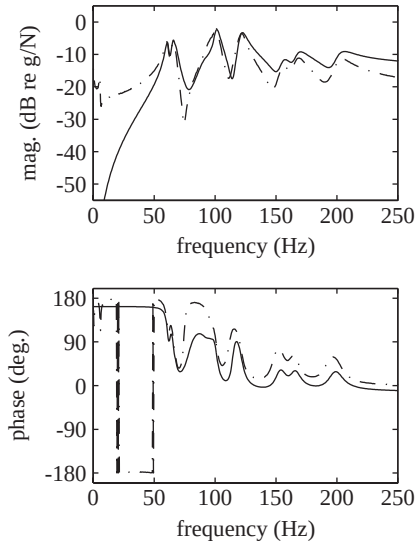

Fig. 23. The driving-point acceleration FRF in the Z-direction reconstructed from the modes (solid line) compared to the original measured FRF (chained line).

4.1. Calculation of four-pole parameters

The four-pole parameters A, B, C and D relate the force F_1 and velocity V_1 at the input end of an isolator to the force F_2 and velocity V_2 at the output end by [11]

$$\begin{Bmatrix} F_1 \\ V_1 \end{Bmatrix} = \begin{bmatrix} A & B \\ C & D \end{bmatrix} \begin{Bmatrix} F_2 \\ V_2 \end{Bmatrix} \tag{3}$$

which is in effect a transfer-matrix formulation. A represents the reciprocal of the force transmissibility when the output end is blocked (zero velocity) and D represents the reciprocal velocity transmissibility when the output end is free (zero force). B represents the impedance between an input force and output velocity when the output is free, while C represents the mobility between an input velocity and an output force when the output is blocked. The four-pole approach considers the translational dynamics of the isolator in only one direction at a time, ignoring other degrees of freedom and any cross-coupling between them. However, the four-pole parameters can be measured relatively easily using a standardised test procedure such as that described in Ref. [12], while giving a more complete dynamic description of an isolator than a single impedance value.

Here the four-pole parameters in the axial (Z) direction will be calculated. Since forces at all four corners of each end plate must be considered in order to obtain single input and output forces, the set of measured FRFs is insufficient and the full reconstructed set must be used. A fair amount of matrix reduction is required to obtain the four-pole parameters from the reconstructed FRFs. The four-pole approach treats only the end forces and velocities, and then assumes that there is only axial motion. To begin the process of reduction, either of the 8×8 FRF matrix equations that result from (1) for the small and medium isolators can be partitioned between the two ends of the particular isolator to give

$$\begin{Bmatrix} \mathbf{X}_1 \\ \mathbf{X}_2 \end{Bmatrix} = \begin{bmatrix} \mathbf{H}_{11} & \mathbf{H}_{12} \\ \mathbf{H}_{21} & \mathbf{H}_{22} \end{bmatrix} \begin{Bmatrix} \mathbf{F}_1 \\ \mathbf{F}_2 \end{Bmatrix} = \begin{bmatrix} \boldsymbol{\alpha} & \boldsymbol{\beta} \\ \boldsymbol{\gamma} & \boldsymbol{\delta} \end{bmatrix} \begin{Bmatrix} \mathbf{F}_1 \\ \mathbf{F}_2 \end{Bmatrix}, \tag{4}$$

where each $\mathbf{X}$ contains four corner displacements and each $\mathbf{F}$ contains four corner forces in the Z-direction. Subscript 1 refers to the input end plate and subscript 2 refers to the output end plate. The $\boldsymbol{\alpha}, \boldsymbol{\beta}, \boldsymbol{\gamma}$ and $\boldsymbol{\delta}$ notation for the partitions is introduced for later convenience. The two-stage isolator has a middle plate as well as the two end ones. Its FRF matrix can be reduced so that only FRFs relating the two ends of the isolator remain. The 12×12 FRF matrix equation arising from Eq. (1) for the two-stage isolator can be partitioned to give

$$\begin{Bmatrix} \mathbf{X}_1 \\ \mathbf{X}_m \\ \mathbf{X}_2 \end{Bmatrix} = \begin{bmatrix} \mathbf{H}_{11} & \mathbf{H}_{1m} & \mathbf{H}_{12} \\ \mathbf{H}_{m1} & \mathbf{H}_{mm} & \mathbf{H}_{m2} \\ \mathbf{H}_{21} & \mathbf{H}_{2m} & \mathbf{H}_{22} \end{bmatrix} \begin{Bmatrix} \mathbf{F}_1 \\ \mathbf{F}_m \\ \mathbf{F}_2 \end{Bmatrix}, \tag{5}$$

where subscript m refers to the middle plate in addition to the subscripts 1 and 2 for the end plates. Since the displacements of the middle plate are not of interest here, the second partition row of Eq. (5) can be removed completely. With the middle plate forces $\mathbf{F}_m$ set to zero, the second partition elements of the first and third partition rows also drop out of the equations. Therefore,

the problem is reduced to a relationship between plates 1 and 2 alone, expressed in the same form as Eq. (4). The following discussion can then be applied to any one of the small, medium or two-stage isolators.

Eq. (4) is cast in terms of vectors of four forces and four displacements at each end of the isolator, whereas the four-pole parameter equation (3) deals with only one scalar force and one scalar velocity at each end. The isolator needs to be restricted to linear axial motion to achieve the state that the four-pole parameters are defined for. Once this is done, the sets of four forces and four displacements can be reduced to single force–velocity pairs. There are two approaches to achieve this restriction, both exactly equivalent for an ideal symmetrical isolator. The first is to assume that all four corner displacements of an end plate are the same; the second is to assume that equal forces are applied to each of the corners of an end plate, resulting in a net force equivalent to a single, centrally applied input force. The first approach is closer to the conditions of the universal test method of Ref. [12] and is used in an earlier paper [2] to calculate four-pole parameters for the two-stage isolator. However, that calculation requires that the FRF matrix is inverted to give a dynamic-stiffness matrix, in order to be able to easily sum the corner forces to get the resultant single force. As they stand, the full FRF matrices for all three isolators overspecify the problem, because only 3 dof (for example, three corner displacements) are required to fully define the axial components of the motion of a rigid end plate. This means that not all the rows of the FRF matrices are linearly independent, the ranks of the matrices are less than their dimensions, and so the matrices are singular and cannot be inverted. The approach works for the two-stage isolator only because of the reduction of the FRF matrix of Eq. (2) to a size where its rank and dimensions are equal. Complicated rearrangement of the equations to remove redundant degrees of freedom and account for the forces acting along them would be needed to be able to obtain dynamic-stiffness matrices for the small and medium isolators.

Therefore the second approach of starting with four equal forces at the four corners of each end plate will be used here. The two-stage isolator's results using this method are different from those in Ref. [2], but probably more reliable. To give a single centrally applied force F_1 acting on the input end, the elements of $\mathbf{F}_1$ in Eq. (4) are all set to $\frac{1}{4}F_1$; likewise, the elements of $\mathbf{F}_2$ are all set to $\frac{1}{4}F_2$ to give a total force of F_2 at the output end. The input and output end displacements, X_1 and X_2 say, are then given by the averages of the four corner displacements at each end, that is, one-quarter of the sums of the elements of $\mathbf{X}_1$ and $\mathbf{X}_2$, respectively. For a perfectly symmetrical isolator, the four corner displacements at an end would all be equal and equal to the corresponding four-pole displacement under the assumed loading conditions—the averaging evens out the effect of irregularities in the real isolators. Applying the two assumptions in turn allows (4) to be simplified to the following 2×2 system:

$$\begin{Bmatrix} X_1 \\ X_2 \end{Bmatrix} = \frac{1}{16}\begin{bmatrix} \sum \alpha_{jk} & \sum \beta_{jk} \\ \sum \gamma_{jk} & \sum \delta_{jk} \end{bmatrix}\begin{Bmatrix} F_1 \\ F_2 \end{Bmatrix} = \begin{bmatrix} \alpha_s & \beta_s \\ \gamma_s & \delta_s \end{bmatrix}\begin{Bmatrix} F_1 \\ F_2 \end{Bmatrix}, \tag{6}$$

where the α_{jk}, β_{jk}, γ_{jk} and δ_{jk} are the elements of the partitions $\boldsymbol{\alpha}, \boldsymbol{\beta}, \boldsymbol{\gamma}$ and $\boldsymbol{\delta}$, respectively in Eq. (4). To convert Eq. (6) into four-pole parameter form requires the substitutions $X_1 = V_1/\mathrm{i}\omega$ and $X_2 = V_2/\mathrm{i}\omega$ to introduce the end velocities V_1 and V_2, and $F_2 = -F_2'$ to change the output force into that which would act on the next element of a four-pole chain instead of the force which acts

on the isolator's end. Making these substitutions in Eq. (6) and rearranging gives

$$\begin{Bmatrix} F_1 \\ V_1 \end{Bmatrix} = \begin{bmatrix} \delta_s/\gamma_s & 16/\mathrm{i}\omega\gamma_s \\ \mathrm{i}\omega(\alpha_s\delta_s - \beta_s\gamma_s)/16\gamma_s & \alpha_s/\gamma_s \end{bmatrix} \begin{Bmatrix} F_2' \\ V_2 \end{Bmatrix} = \begin{bmatrix} A & B \\ C & D \end{bmatrix} \begin{Bmatrix} F_2' \\ V_2 \end{Bmatrix} \tag{7}$$

which is of the same form as Eq. (3).

The axial four-pole parameters for the three isolators can now be calculated by reconstructing the FRF matrix for each one using Eq. (2), then following the procedure outlined in Eqs. (4)–(7). The final results, calculated using MATLAB, are plotted in Figs. 24–26. Parameters A and D are nearly equal for each isolator, equality of these two parameters being a feature of a symmetric isolator (one that behaves the same dynamically when the input and output ends are swapped) [11]. For the small and medium isolators, Figs. 24 and 25, A and D vary only slightly from unity (0 dB). A massless isolator would have $A = D = 1$, but would also have $B = 0$ [11], which latter condition is clearly not the case here. The small and medium isolators each have two identical end plates separated by one or more rubber elements, which with their relatively low mass act like massless springs. Thus force must be transmitted identically when the output is blocked. When the output is free, both ends move in the same way even at the axial resonance (albeit with greater amplitude then), so the ratio of their velocities remains unity. On the other hand, A and D for the two-stage isolator, Fig. 26, show a dip at 167 Hz. This corresponds to the symmetric translation mode (number 9 in Table 9), where the middle plate, as well as the end plates, is moving in resonance. The inertia of the middle plate serves to increase the force or velocity (as the case may be) transmitted to the output. Elsewhere in the frequency range shown the middle plate is stationary and A and D are unity.

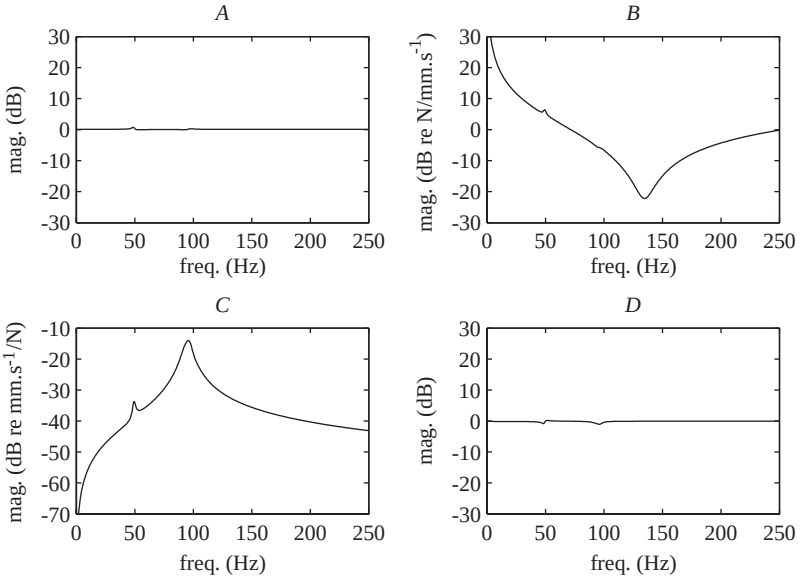

Fig. 24. The magnitudes of the four-pole parameters A, B, C and D for the small isolator calculated from its reconstructed FRFs for the Z-direction.

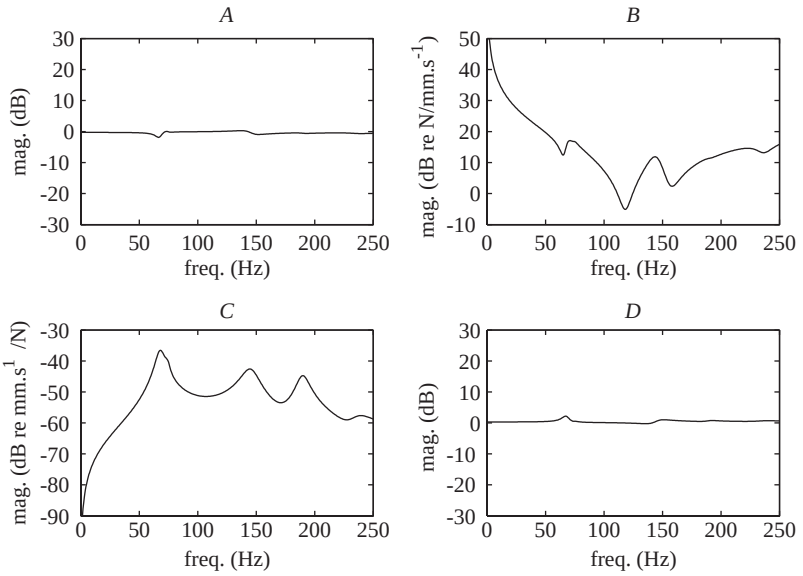

Fig. 25. The magnitudes of the four-pole parameters A, B, C and D for the medium isolator calculated from its reconstructed FRFs for the Z-direction.

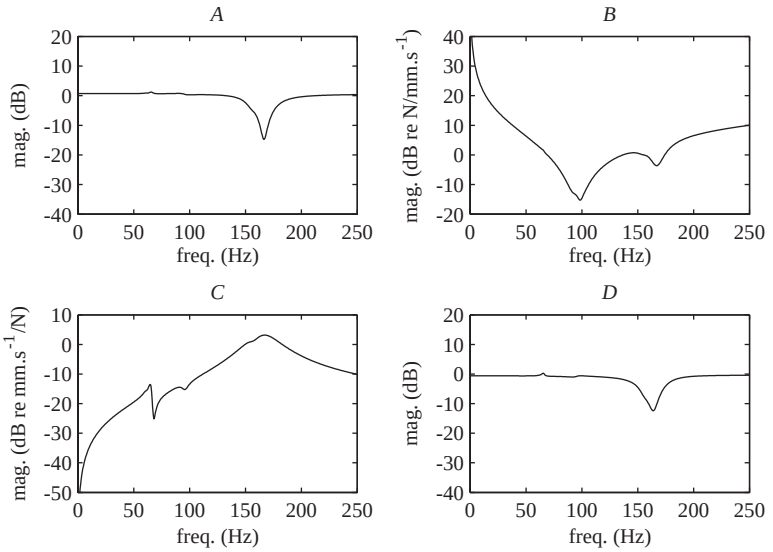

Fig. 26. The magnitudes of the four-pole parameters A, B, C and D for the two-stage isolator calculated from its reconstructed FRFs for the Z-direction.

It is interesting to note which modes correspond to the peaks or dips in the other two parameters B and C. For the small isolator, Fig. 24, B has a prominent dip at 134 Hz, the axial translation mode, while C has a prominent peak at 95 Hz, the rotation about Y mode. The mixed

modes of the medium isolator show up strongly in Fig. 25: B has dips at every mode *except* the 74 Hz equal tilting about Y and 157 Hz rotation about X, and C has peaks at every mode *except* the 118 Hz rotation about Y and the 157 Hz rotation about X. Curiously, C also has a peak at 145 Hz, which does not correspond to any of the modes observed for the medium isolator. The results for the two-stage isolator, Fig. 26, show the influence of fewer modes. B has its most prominent dip with components at both the 93 Hz antisymmetric translation in Z and 101 Hz antisymmetric rotation about Y, with a secondary dip at the 167 Hz symmetric translation in Z mode. C shows some influence of the equal-tilting modes around 64 Hz, but the main peak is made up of the 155 Hz symmetric rotation about Y and, once again, the 167 Hz symmetric translation in Z. It is not clear why modes which are not purely axial translation can appear so strongly, particularly in the case of the medium isolator, under the condition of centrally applied forces. The answer lies at least in part with physical asymmetries of the isolators analysed, allowing four equal corner forces to induce non-translational modes.

4.2. Calculation of transmissibilities

Transmissibilities are usually defined as the ratio of the velocity at one point of a structure to the velocity at another point. In the frequency domain, this is the same as the ratio of the corresponding displacements or accelerations, as any $i\omega$ factors cancel. Since the boundary conditions and applied loading can be specified in any way, the definition of a transmissibility tends to be somewhat arbitrary: many different transmissibilities between the same two points become possible. A transmissibility is thus only really useful as an indication of the dynamics of a structure in a specific situation, not as a general characterisation.

In the current discussion, the axial dynamics of the isolators are of interest. Here a transmissibility will be defined as the ratio of an output velocity to an input velocity in the same direction. The input end of the isolator is that which has the (single) input force applied to it, while the output end is the opposite end of the isolator. The isolator is otherwise unconstrained and free.

The axial transmissibility of an isolator with a force applied centrally to one end is given by the reciprocal of the four-pole parameter D. Thus the transmissibilities with this force input for the small, medium and two-stage isolators are given by the negative values in dB (since the dB scale is logarithmic) of the parameters D plotted in Figs. 24–26, respectively. The axial transmissibilities of the small and medium isolators are therefore unity, and that of the two-stage isolator is also unity for most of the frequency range up to 250 Hz, but with a resonance at the 167 Hz symmetric translation mode.

The axial transmissibility of an isolator with an axial force applied off-centre is more complicated to define. Whereas a central force is assumed to induce only axial translation in these symmetrical isolators, an off-centre force is equivalent to the central force plus two moments, one acting about the X-axis, the other about the Y-axis. These moments induce rotations and so the total motion in the axial direction must be described in terms of 3 dof. The most intuitive are perhaps the translation in the Z-direction of the centre of an end plate, the rotation about its X-axis, and the rotation about its Y-axis. These 3 dof can be denoted by the displacements W, Θ

and Φ, respectively. Transmissibilities in all three should be considered if a reasonable part of the overall picture of the isolator's response is to be obtained.

Since the four corner displacements of an end plate include a redundant coordinate, it is easiest to write them in terms of the three independent degrees of freedom and then solve for W, Θ and Φ. While it is possible to get a pair of solutions in each case, each solution involving only two corner displacements and theoretically equivalent, it is better to include all four corner displacements in a single solution for each of W, Θ and Φ to average out differences that exist in the actual results. Assuming small angular displacements, the solutions for the input plate are

$$\begin{aligned} W &= (X_1 + X_2 + X_3 + X_4)/4, \\ \Theta &= (-X_1 - X_2 + X_3 + X_4)/2l, \\ \Phi &= (X_1 - X_2 - X_3 + X_4)/2l, \end{aligned} \tag{8}$$

where X_1, X_2, X_3 and X_4 are the elements of $\mathbf{X}_1$ in Eq. (4) and l is the sidelength of the square end plate. Similar equations can be written for the displacement and rotations of the output end plate. With the off-centre input force applied at corner 1, $F_1 = F$ and $F_j = 0$ for all other corners j (including at the output end), resulting in $X_j = H_{j1}F$ for all the corner displacements, where H_{j1} represents the jth element of the first column of the whole FRF matrix in Eq. (4). These H_{j1} FRFs happen to correspond to the FRFs that were measured. Substituting FRF expressions for the X_j in Eq. (8) and the corresponding equations for the output end, then taking the ratios of each displacement and rotation, gives

$$\begin{aligned} T_W &= \frac{H_{51} + H_{61} + H_{71} + H_{81}}{H_{11} + H_{21} + H_{31} + H_{41}}, \\ T_\Theta &= \frac{-H_{51} - H_{61} + H_{71} + H_{81}}{-H_{11} - H_{21} + H_{31} + H_{41}}, \\ T_\Phi &= \frac{H_{51} - H_{61} - H_{71} + H_{81}}{H_{11} - H_{21} - H_{31} + H_{41}}, \end{aligned} \tag{9}$$

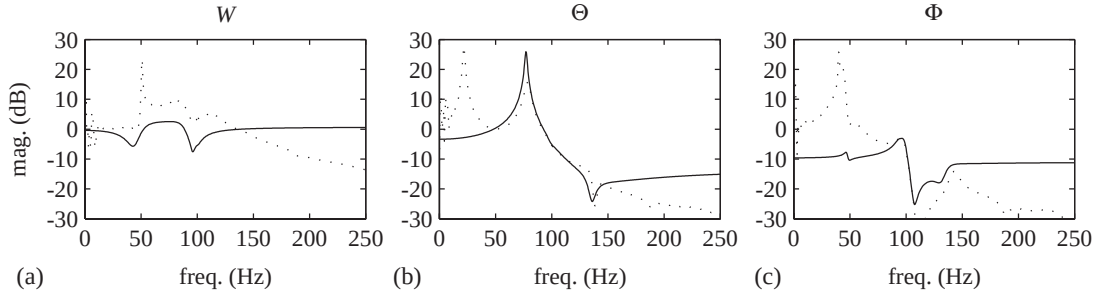

Fig. 27. The magnitudes of the axial transmissibilities of the small isolator with an off-centre load applied at A1, showing transmissibilities for (a) translation in Z, (b) rotation about X, and (c) rotation about Y. Results calculated using reconstructed FRFs (solid lines) are compared to those using the measured FRFs (dotted lines).

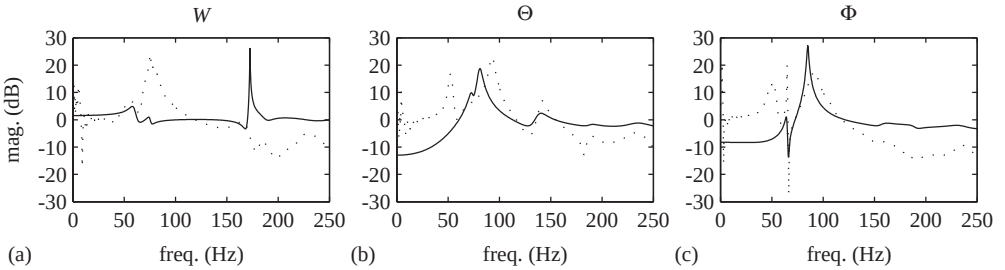

Fig. 28. The magnitudes of the axial transmissibilities of the medium isolator with an off-centre load applied at A1, showing transmissibilities for (a) translation in Z, (b) rotation about X, and (c) rotation about Y. Results calculated using reconstructed FRFs (solid lines) are compared to those using the measured FRFs (dotted lines).

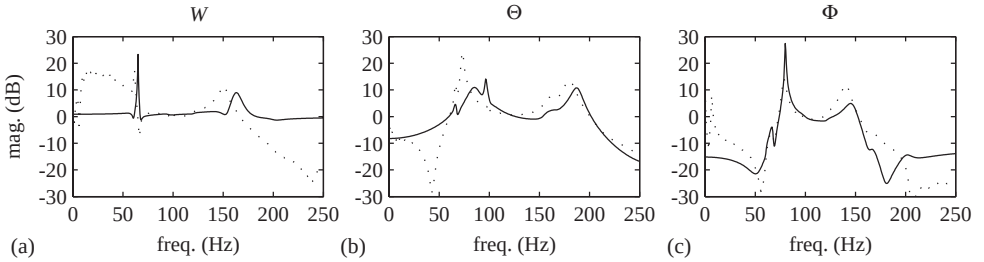

Fig. 29. The magnitudes of the axial transmissibilities of the two-stage isolator with an off-centre load applied at A1, showing transmissibilities for (a) translation in Z, (b) rotation about X, and (c) rotation about Y. Results calculated using reconstructed FRFs (solid lines) are compared to those using the measured FRFs (dotted lines).

where T_W, T_Θ and T_Φ are the transmissibilities in W, Θ and Φ, respectively, and the subscripts 5, 6, 7 and 8 refer to the four corners of the output end plate.

The transmissibilities calculated from Eqs. (9) using both reconstructed and measured FRFs are plotted in Figs. 27, 28 and 29 for the small, medium and two-stage isolators, respectively. In each case, the peaks and troughs of the transmissibilities sometimes correspond to modes observed for the relevant isolator, but often not. For example, the axial translation transmissibility for the small isolator calculated from reconstructed FRFs in Fig. 27(a) has troughs at about 43 and 96 Hz. While the latter corresponds quite closely to the rotation about Y mode (number 3 in Table 3), the former is several Hz away from the nearest mode observed, the 49 Hz rotation about X (number 1 in Table 3).

It can also be seen that the transmissibilities calculated from the measured FRFs (the dotted lines in the figures) quite often differ significantly from the ones based on reconstructed FRFs (the solid lines). Often the differences are ones of magnitude, with both transmissibilities displaying broadly similar peak and trough frequencies, but there are also several peaks appearing on the results based on measurements that do not appear on the reconstructed ones, and that are not low-frequency response due to modified rigid-body modes. It should also be noted that

calculating the transmissibilities using either of the alternative solutions mentioned above gives results that can vary widely in the magnitudes of their peaks and troughs too. Given these observations, which point to physical irregularities in theoretically symmetrical isolators, it would be expected that the transmissibilities would also be different if the input force was applied to a different corner of the input end plate. It is therefore difficult to be able to claim a definitive axial transmissibility (or set of three) when one of these isolator models is loaded with an off-centre force.

5. Conclusions

The modal properties of two single-stage vibration isolator models and one two-stage vibration isolator model have been extracted from FRFs measured in the three principal directions with the isolators suspended in such a way as to approximate the free–free state. This approach allows the full dynamics of each isolator to be observed, with no restrictions on coupling between directions and no constraints on any degrees of freedom. The results show a large number of modes of various types with natural frequencies up to about 240 Hz in the low-frequency range examined, where the steel plates of the isolators can be assumed to be rigid. Many of the modes observed did not fit into the simple scheme of modes that might have been expected, particularly in the medium isolator's case. Although the measurements in the three directions were done separately for each isolator, comparing the three sets of results in each case reveals that several modes manifest motion in more than one of the principal directions. This is due to significant coupling between rotational and translational degrees of freedom, which arises from the way that the deformed rubber elements transmit forces between the plates.

It has been demonstrated how the four-pole parameters for an isolator can be obtained via a straightforward procedure that condenses the information in the full FRF matrix derived from the modal properties. This would allow a partial comparison of the results of modal analysis to other work based on the four-pole approach. However, the four-pole approach as currently formulated is somewhat limited. It considers only translational motion in the three principal directions, and assumes that coupling between them is negligible. In fact, as shown by the modal results presented in this paper, rotational degrees of freedom and coupling between directions are major features of the dynamics of the three isolators considered. Since it is conceivable that many degrees of freedom could be involved in the motion of a complex machine–isolator–foundation system with many isolators, these features must be taken into account.

Axial transmissibilities of the isolators for a centrally applied force follow directly from the four-pole parameters. Since the transmissibility is unity for the two single-stage isolators and contains just one resonance at the symmetric axial translation mode for the two-stage isolator, not a lot of information is provided by this type of characterisation. It has been shown that problems arise in attempting to define transmissibility with an off-centre force, because a single axial translation transmissibility is no longer sufficient to describe what is going on, as well as the fact that several different values for any given transmissibility defined are possible for a real, not perfectly symmetrical isolator. A full description, such as an FRF matrix, is therefore the only

way to properly describe the dynamics of these small-scale isolator models, capturing all effects including those due to coupling and physical asymmetries.

Appendix A. Numerical data for the mode shapes

The mode-shape data that follows is presented as the real and imaginary parts of the elements of the modal vectors for each mode. These elements correspond to the measurement positions or

Table 10
Mode-shape data for the small isolator from *X*-direction measurements

Coord.	Mode 1: $f_n = 39.9$ Hz, $\eta_n = 0.0633$		Mode 2: $f_n = 100.6$ Hz, $\eta_n = 0.0867$	
	Re	Im	Re	Im
A2	0.274538	−0.030862	0.148422	−0.011037
A3	−0.300195	0.019272	0.151011	0.008128
B2	−0.221252	−0.030505	−0.167607	−0.021415
B3	0.320639	−0.016194	−0.142369	0.002964

Table 11
Mode-shape data for the small isolator from *Y*-direction measurements

Coord.	Mode 1: $f_n = 39.8$ Hz, $\eta_n = 0.0594$		Mode 2: $f_n = 94.4$ Hz, $\eta_n = 0.1137$	
	Re	Im	Re	Im
A3	0.269949	−0.020885	0.133301	−0.024530
A4	−0.289953	0.037167	0.234945	−0.007030
B3	−0.173742	−0.008901	−0.103054	−0.013013
B4	0.275827	−0.034350	−0.173308	−0.011156

Table 12
Mode-shape data for the small isolator from *Z*-direction measurements

Coord.	Mode 1: $f_n = 49.1$ Hz, $\eta_n = 0.0650$		Mode 2: $f_n = 93.1$ Hz, $\eta_n = 0.0760$		Mode 3: $f_n = 95.8$ Hz, $\eta_n = 0.0705$		Mode 4: $f_n = 99.6$ Hz, $\eta_n = 0.0675$		Mode 5: $f_n = 134.3$ Hz, $\eta_n = 0.1046$	
	Re	Im	Re	Im	Re	Im	Re	Im	Re	Im
A1	0.342124	−0.029623	0.447993	−0.015807	0.217074	0.068751	0.256342	−0.011723	0.325077	0.040731
A2	0.387510	−0.030292	0.161188	0.043418	−0.588190	0.132890	−0.290969	−0.008475	0.341565	0.034073
A3	−0.380485	0.056372	−0.488945	0.054147	−0.276537	−0.043477	−0.263028	−0.001841	0.341859	0.024215
A4	−0.390439	0.050409	−0.137762	−0.009689	0.524637	−0.104029	0.288339	−0.005289	0.341684	0.032129
B1	−0.369350	0.036365	0.107495	−0.004670	−0.444634	0.153184	0.357197	0.000976	−0.366542	−0.047320
B2	−0.369810	0.024158	0.470774	−0.019903	0.184768	−0.001284	−0.384713	0.014061	−0.345129	−0.026481
B3	0.387393	−0.032516	−0.118272	−0.006088	0.474578	−0.131642	−0.370512	0.003099	−0.308324	−0.045244
B4	0.399675	−0.043823	−0.485515	0.011212	−0.160038	0.010338	0.374801	−0.001457	−0.335151	−0.063045

Table 13
Mode-shape data for the medium isolator from *X*-direction measurements

Coord.	Mode 1: $f_n = 60.9$ Hz, $\eta_n = 0.1130$		Mode 2: $f_n = 64.0$ Hz, $\eta_n = 0.0366$		Mode 3: $f_n = 74.4$ Hz, $\eta_n = 0.0594$		Mode 4: $f_n = 116.3$ Hz, $\eta_n = 0.1020$	
	Re	Im	Re	Im	Re	Im	Re	Im
A2	0.213244	0.005839	0.052306	0.011081	0.030330	0.008111	0.027738	0.002839
A3	−0.121400	−0.006509	−0.040507	−0.004500	0.125296	−0.044059	−0.035013	0.025600
B2	−0.179772	−0.010637	−0.036813	−0.009993	−0.029712	−0.009618	−0.020787	−0.003118
B3	0.119810	0.002820	0.042151	0.002096	−0.117759	0.037889	0.026033	−0.020579

Table 14
Mode-shape data for the medium isolator from *Y*-direction measurements

Coord.	Mode 1: $f_n = 62.6$ Hz, $\eta_n = 0.1586$		Mode 2: $f_n = 64.6$ Hz, $\eta_n = 0.0669$		Mode 3: $f_n = 75.5$ Hz, $\eta_n = 0.0580$		Mode 4: $f_n = 102.4$ Hz, $\eta_n = 0.0775$	
	Re	Im	Re	Im	Re	Im	Re	Im
A3	0.131394	0.034097	0.134595	−0.007767	0.053792	−0.016007	0.019099	−0.004123
A4	−0.174912	−0.018571	0.093607	0.063450	−0.049128	0.004936	0.026274	−0.000722
B3	−0.128269	−0.037077	−0.138960	−0.000437	−0.057976	0.012782	−0.025875	0.002052
B4	0.190696	0.018613	−0.073523	−0.071670	0.042353	−0.000251	−0.029919	0.010837

Table 15
Mode-shape data for the medium isolator from *Z*-direction measurements

Coord.	Mode 1: $f_n = 65.7$ Hz, $\eta_n = 0.0794$		Mode 2: $f_n = 74.4$ Hz, $\eta_n = 0.0633$		Mode 3: $f_n = 118.2$ Hz, $\eta_n = 0.0758$		Mode 4: $f_n = 156.6$ Hz, $\eta_n = 0.0798$		Mode 5: $f_n = 189.8$ Hz, $\eta_n = 0.0585$		Mode 6: $f_n = 236.3$ Hz, $\eta_n = 0.0651$	
	Re	Im	Re	Im	Re	Im	Re	Im	Re	Im	Re	Im
A1	0.078707	−0.039962	0.117013	−0.015027	0.317619	0.025035	0.140090	−0.003008	0.046273	−0.003496	0.085214	−0.059258
A2	0.110992	0.032811	−0.093997	0.002644	0.041871	0.014080	0.153710	0.008866	0.055038	0.000631	0.046234	−0.034238
A3	−0.129090	0.022048	−0.125944	0.011356	−0.140774	−0.004077	−0.296135	0.001782	−0.033771	0.005133	−0.049501	0.034547
A4	−0.147230	−0.059308	0.120026	−0.007118	0.178533	0.014167	−0.299158	−0.013856	−0.012257	−0.004905	0.012640	0.000734
B1	0.170872	−0.009002	0.125125	−0.006245	−0.314155	−0.034078	−0.152305	−0.002143	−0.043826	−0.001190	−0.088912	0.058491
B2	0.188479	0.074095	−0.145832	0.013222	−0.016655	−0.010952	−0.135098	−0.009494	−0.056984	0.000499	−0.046862	0.032887
B3	−0.136175	0.016161	−0.134397	0.007568	0.116347	0.006432	0.281106	0.005482	0.026393	−0.002427	0.048382	−0.031275
B4	−0.155266	−0.063670	0.126596	−0.011973	−0.186103	−0.012983	0.273310	0.014834	0.043753	−0.001072	0.007028	−0.006252

coordinates. The natural frequency and modal damping of each mode are also repeated here for convenience. Data for the small isolator appears in Tables 10–12; data for the medium isolator in Tables 13–15; and data for the two-stage isolator in Tables 16–18.

Table 16
Mode-shape data for the two-stage isolator from X-direction measurements

Coord.	Mode 1: $f_n = 47.2$ Hz, $\eta_n = 0.0464$		Mode 2: $f_n = 65.5$ Hz, $\eta_n = 0.0596$		Mode 3: $f_n = 67.5$ Hz, $\eta_n = 0.0518$		Mode 4: $f_n = 82.3$ Hz, $\eta_n = 0.0528$		Mode 5: $f_n = 101.7$ Hz, $\eta_n = 0.0601$	
	Re	Im	Re	Im	Re	Im	Re	Im	Re	Im
A2	0.148319	−0.000699	0.087695	0.003079	0.078209	−0.005558	0.088356	−0.001707	0.022650	−0.006682
A3	−0.146960	0.009399	0.129376	−0.006619	0.055273	0.001192	−0.083663	0.004128	0.069952	−0.005090
B2	0.003857	0.000395	0.006492	−0.019129	−0.148958	0.015024	−0.173424	0.000780	−0.096846	0.012425
B3	0.000801	−0.000284	0.008623	−0.008741	−0.150410	0.006736	0.162480	−0.007131	−0.111150	0.002276
C2	−0.152578	0.001974	−0.127818	0.013774	0.089256	−0.011012	0.083647	−0.000198	0.046453	−0.007254
C3	0.141014	−0.011442	−0.111219	0.010514	0.099510	−0.007881	−0.082061	0.004672	0.041031	0.001901

Table 17
Mode-shape data for the two-stage isolator from Y-direction measurements

Coord.	Mode 1: $f_n = 47.2$ Hz, $\eta_n = 0.0470$		Mode 2: $f_n = 61.0$ Hz, $\eta_n = 0.0576$		Mode 3: $f_n = 67.9$ Hz, $\eta_n = 0.0548$		Mode 4: $f_n = 82.1$ Hz, $\eta_n = 0.0570$		Mode 5: $f_n = 121.3$ Hz, $\eta_n = 0.0726$	
	Re	Im	Re	Im	Re	Im	Re	Im	Re	Im
A3	0.167181	−0.002508	0.104599	−0.007363	0.097347	−0.002129	0.105418	−0.001846	0.024651	−0.004204
A4	−0.175491	0.011256	0.118203	−0.007273	0.092944	−0.003215	−0.103892	0.004118	−0.031067	0.003635
B3	0.003811	0.000667	−0.008224	−0.009236	−0.157106	−0.001040	−0.203779	0.003389	0.033356	0.012683
B4	−0.000816	0.000012	0.016769	−0.000230	−0.181299	0.022488	0.191223	−0.006479	0.043873	−0.005909
C3	−0.165578	0.009004	−0.145395	0.008177	0.067599	−0.003497	0.111603	−0.008226	−0.023264	−0.006368
C4	0.171994	−0.011463	−0.109964	−0.002349	0.097389	−0.018646	−0.089848	0.004265	−0.009169	0.002001

Table 18
Mode-shape data for the two-stage isolator from Z-direction measurements

Coord.	Mode 1: $f_n = 61.1$ Hz, $\eta_n = 0.0515$		Mode 2: $f_n = 65.7$ Hz, $\eta_n = 0.0517$		Mode 3: $f_n = 67.6$ Hz, $\eta_n = 0.0526$		Mode 4: $f_n = 93.0$ Hz, $\eta_n = 0.1110$		Mode 5: $f_n = 98.3$ Hz, $\eta_n = 0.0796$	
	Re	Im	Re	Im	Re	Im	Re	Im	Re	Im
A1	0.136143	−0.012527	0.146102	−0.010358	0.087730	0.003122	0.100289	−0.060674	0.129559	−0.098823
A2	0.154867	−0.028934	−0.164663	0.025612	−0.063740	0.016315	0.074889	−0.165016	0.093752	−0.139262
A3	−0.148215	0.018366	−0.173896	0.014920	−0.093222	−0.005875	0.046298	−0.133994	0.096903	−0.104939
A4	−0.134331	0.025123	0.145541	−0.019159	0.048197	−0.009746	0.081199	−0.050149	0.148385	−0.088122
B1	0.129981	−0.014489	0.116319	−0.012948	−0.022336	0.032382	−0.000880	0.002478	0.003974	0.001004
B2	0.147355	−0.025421	−0.120249	0.021628	0.023447	−0.008311	0.012445	−0.006520	0.004674	−0.010870
B3	−0.136868	0.017337	−0.126666	0.013796	0.007260	−0.030352	0.001663	0.002231	0.001345	−0.001354
B4	−0.172477	0.014407	0.137590	−0.006999	0.015830	−0.001492	0.024703	−0.004567	0.029508	−0.012834
C1	0.144819	−0.027307	0.133416	−0.032486	−0.090492	0.082971	−0.099659	0.080794	−0.102752	0.100171
C2	0.169441	−0.036441	−0.126099	0.035136	0.094716	−0.042390	−0.080002	0.208187	−0.071750	0.186388
C3	−0.152678	0.028013	−0.136856	0.034830	0.107873	−0.091290	−0.041991	0.164920	−0.092406	0.136627
C4	−0.151359	0.027920	0.106693	−0.029293	−0.081014	0.033780	−0.070592	0.067998	−0.131239	0.078692
Coord.	Mode 6: $f_n = 100.6$ Hz, $\eta_n = 0.0558$		Mode 7: $f_n = 121.2$ Hz, $\eta_n = 0.0621$		Mode 8: $f_n = 155.3$ Hz, $\eta_n = 0.0703$		Mode 9: $f_n = 166.9$ Hz, $\eta_n = 0.0658$		Mode 10: $f_n = 200.8$ Hz, $\eta_n = 0.0743$	
	Re	Im	Re	Im	Re	Im	Re	Im	Re	Im
A1	0.212684	0.016378	0.197625	−0.010955	0.101135	−0.009811	0.108258	0.000754	0.115685	−0.003072
A2	−0.140422	0.033450	0.229591	−0.024006	−0.160843	0.006675	0.068158	−0.014344	0.127326	−0.012014
A3	−0.131111	0.032113	−0.214841	0.010530	−0.151151	0.012116	0.049895	−0.009726	−0.125675	0.003741
A4	0.231134	0.022964	−0.208157	0.009079	0.105180	0.002768	0.102402	0.000291	−0.118863	0.002627
B1	0.009512	0.002580	0.008677	−0.002451	−0.204778	0.018991	−0.217814	0.004870	−0.237271	0.010275
B2	−0.005689	0.001076	0.000917	0.000056	0.337345	−0.058023	−0.107732	0.035481	−0.260904	0.036231
B3	−0.001861	−0.000419	−0.005081	0.001849	0.297036	−0.036018	−0.092408	0.022831	0.257613	−0.012828
B4	0.024422	0.013072	−0.012088	−0.007195	−0.262327	0.019404	−0.248332	−0.013085	0.266772	−0.020606
C1	−0.206374	0.005244	−0.219107	0.023060	0.080997	0.002421	0.100832	−0.004962	0.123349	0.002765
C2	0.116397	−0.036503	−0.241996	0.039933	−0.151488	0.031975	0.053564	−0.016881	0.135477	−0.013830
C3	0.108572	−0.043129	0.231561	−0.020133	−0.127169	0.006994	0.051282	−0.012178	−0.132659	0.000966
C4	−0.214830	−0.007089	0.221141	−0.020667	0.101151	−0.014437	0.109911	−0.005356	−0.128985	0.007516

References

[1] J.A. Forrest, Free–free dynamics of some vibration isolators, in: A. Zander (Ed.), *Acoustics 2002*, Australian Acoustical Society, Adelaide, Australia, 2002, pp. 406–416.
[2] J.A. Forrest, Experimental modal analysis of a two-stage vibration isolator model, in: J. Mathew (Ed.), *10th Asia-Pacific Vibration Conference (APVC 2003)*, Vol. I, Queensland University of Technology, Gold Coast, Queensland, Australia, 2003, pp. 127–132.
[3] Y. Tso, J. Forrest, C. Norwood, Foundation design methods for ship noise reduction, in: L. Prandolini (Ed.), *Pacific 2002 International Maritime Conference*, Institution of Engineers, Australia, Sydney, Australia, 2002, pp. 56–65.
[4] D.J. Ewins, *Modal Testing: Theory, Practice and Application*, second ed., Research Studies Press, Baldock, Hertfordshire, England, 2000.
[5] L. Meirovitch, *Elements of Vibration Analysis*, second edition, McGraw-Hill, New York, 1986.
[6] P.B. Lindley, Engineering design with natural rubber, NR Technical Bulletin, Malaysian Rubber Producers' Research Association, Welwyn Garden City, Herts, UK, 1964.
[7] L. Kari, P. Eriksson, B. Stenberg, On the temperature dependence of vibration isolator stiffness in the audible frequency range, in: G. Guidati, H. Hunt, H. Heller, A. Heiss (Eds.), *Seventh International Congress on Sound and Vibration (ICSV7)*, Vol. V, International Institute of Acoustics and Vibration, Garmisch-Partenkirchen, Germany, 2000, pp. 2947–2954.
[8] J.D. Dickens, Phase velocity of rubber element in vibration isolator under static load, *Journal of Sound and Vibration* 234 (2000) 21–42.
[9] R.L. Warley, Dynamic properties of elastomers as related to vibration isolator performance, *Rubber World* 213 (1996) 33–39.
[10] J.W. Verheij, Multi-path Sound Transfer From Resiliently Mounted Shipboard Machinery, PhD Thesis, TNO-TH, Delft, Netherlands, 1982.
[11] C.J. Norwood, J.D. Dickens, The effect of vibration isolator properties and structural stiffness on isolator performance, *Journal of Vibration and Control* 4 (1998) 253–275.
[12] J.D. Dickens, C.J. Norwood, Universal method to measure dynamic performance of vibration isolators under static load, *Journal of Sound and Vibration* 244 (2001) 685–696.
[13] Anon., The fundamentals of modal testing, Application Note 243-3, Hewlett-Packard, Palo Alto, California, USA, 1986.